

# Efficient calculation of Green’s functions on quantum computers via simultaneous circuit perturbation

Samuele Piccinelli,<sup>1,2,\*</sup> Francesco Tacchino,<sup>1,†</sup> Ivano Tavernelli,<sup>1</sup> and Giuseppe Carleo<sup>2</sup>

<sup>1</sup>*IBM Quantum, IBM Research Europe - Zurich, CH-8803 Rüschlikon, Switzerland*

<sup>2</sup>*Institute of Physics, École Polytechnique Fédérale de Lausanne (EPFL), CH-1015 Lausanne, Switzerland*

(Dated: May 12, 2025)

We propose a novel, ancilla-free algorithm to compute Retarded Green’s Functions (RGFs) on quantum computers. Our proposal is based on real-time evolution and specifically designed circuit components, which we refer to as circuit perturbations, acting as a direct representation of the external perturbative force within the quantum circuit in a linear response framework. First, we establish a direct analytical connection between the evaluation of circuit derivatives and the computation of RGFs. We then build on this connection to devise a new approach involving multiple simultaneous time perturbations. Our method does not require long-range connections and is efficient in terms of circuit calls, allowing us to compute the RGFs at different times simultaneously. We benchmark the protocol on the one-dimensional Heisenberg and Fermi–Hubbard models, comparing the resulting dynamical correlations and spectral functions with exact diagonalization. The results demonstrate good quantitative agreement with the predicted solutions even under realistic noise models, highlighting the practical potential of our method for studying complex dynamical phenomena on near-term quantum devices.

## I. INTRODUCTION

Understanding the dynamical properties of quantum many-body systems is a central question in virtually all areas of modern physical sciences, including quantum chemistry, condensed matter and high-energy physics. In particular, the study of low-energy excitations often provides a direct bridge between theoretical models and experimental practice. However, because of the strongly correlated nature of many relevant models and the associated rapid growth of entanglement during time evolution, their investigation remains challenging at large scale. In the last decade, quantum computers have emerged as a promising computational paradigm to address this class of problems [1–3], and recent demonstrations of quantum simulations at the so-called quantum utility scale [4] have opened the way to the use of digital quantum information processing platforms as concrete research tools for the natural sciences.

In this context, time correlation functions of the form

$$\mathcal{C}(t - t_0) = \text{Tr}[\rho A(t) B(t_0)] \quad (1)$$

with  $t > 0$  are particularly useful to characterize the behavior of the systems under study. In the equation above,  $\rho$  is a reference many-body state and  $A, B$  are operators associated with a particular physical process. These time correlation functions are intimately connected to Green’s functions, which connect theoretical predictions with experimental observables, ranging from dynamical modes and spectral functions to scattering amplitudes. The ability to compare theoretical predictions based on these

functions against techniques like angle-resolved photoemission or inelastic neutron scattering constitutes a powerful tool in the hands of computational quantum scientists. Nevertheless, computing dynamical correlation functions in large-scale quantum systems remains a significant challenge for classical simulation techniques.

For these reasons, quantum algorithms to compute Green’s functions in both the time and frequency domains have been extensively explored in the literature [5–8]. Examples include quantum subspace expansion algorithms [9], a generalization of the quantum Equation-of-Motion (qEOM) protocol leveraging the computation of excited states [10–12], variations of the Lanczos algorithm [13, 14] and the continued fraction representations of dynamical correlation functions [15]. In the time domain, a standard approach is to use a suitable version of the well-known ancilla-based Hadamard test [16, 17], which requires long-range controlled quantum operations. While measurements of out-of-time-ordered correlators have been demonstrated on analog quantum simulators [18], large-scale simulations on digital platforms have remained limited, particularly on architectures with restricted qubit-qubit connectivity. Proof-of-principle demonstrations on digital devices include examples based on real-time dynamics [16, 19, 20], imaginary-time dynamics [6, 21] and variational approaches [22–24].

Alternative strategies to access dynamical susceptibilities without requiring ancilla qubits have been explored [25, 26], and, in particular, methods inspired by linear response experiments have been recently proposed [27, 28]. Building on this framework, we construct a novel class of ancilla-free quantum algorithms for Green’s functions. More specifically, we develop and extend the theoretical analysis of previous studies to fully uncover the direct connection between response functions and quantum circuit derivatives. We then leverage such formulation to design a shot-effective pro-

---

\* samuele.piccinelli@ibm.com

† fta@zurich.ibm.com

tolocal based on parallel in time perturbations, stochastic gradient estimation and randomized circuit compilation. Our techniques can be employed to reconstruct dense representations of time correlations with a reduced number of quantum circuit calls compared to sequential alternatives. This, in turn, allows us to extract dynamical structure factors and other spectroscopic properties in a robust and efficient way.

The manuscript is organized as follows. In Section II, we provide an overview of the theoretical framework for linear response theory, laying the foundation for our approach and establishing a unified formalism. In Section III, we present our main contributions. In Section IV, we review the models and the analytical expressions of the quantities used to demonstrate our techniques; subsequently, in Section V, we present and analyze the results of our simulations. Finally, in Section VI, we offer concluding remarks. Although we focus on reference toy models as examples, our results remain general and do not rely on any specific physical system. Throughout this work,  $\hbar$  is set to 1.

## II. BACKGROUND

Let  $H_0$  be the Hamiltonian describing a system in isolation and  $H = H_0 + H_s(t)$  be the total Hamiltonian for the system weakly coupled to an external time-dependent perturbation (or *source*)  $H_s(t)$  that can be turned on and off adiabatically. Let us consider the expectation value  $\langle o_{\mathbf{R}} \rangle = \langle \psi_0 | o_{\mathbf{R}} | \psi_0 \rangle$  of a local observable  $o_{\mathbf{R}}$ , evaluated on the ground state  $|\psi_0\rangle$  of  $H_0$ . Here  $\mathbf{R}$  indicates a generic 3D coordinate in the system and could be, for instance, a specific lattice site if the model is discretized. The source Hamiltonian can be further specified as

$$H_s(t') = \int s(\mathbf{r}', t') o_{\mathbf{r}'}(t') d\mathbf{r}', \quad (2)$$

assuming that the external perturbation couples linearly to the system operators  $o_{\mathbf{r}'}(t')$  at positions  $\mathbf{r}'$  through the force function  $s(\mathbf{r}', t')$ . Moving into the interaction picture, the operator  $o_{\mathbf{R}}$  evolves under the action of the unperturbed Hamiltonian  $H_0$  according to  $o_{\mathbf{R}}^I(t) = e^{iH_0 t} o_{\mathbf{R}} e^{-iH_0 t}$ . Meanwhile, the propagator for quantum states is given by the time-ordered exponential

$$U_s(t, t_0) = \mathcal{T} \exp \left( -i \int_{t_0}^t H_s^I(t') dt' \right), \quad (3)$$

where the interaction-picture source term is defined as  $H_s^I(t') = e^{iH_0 t'} H_s(t') e^{-iH_0 t'}$ .

The evolution in time of  $\langle o_{\mathbf{R}} \rangle$  induced by the action of the source can then be written as

$$\langle o_{\mathbf{R}}(t) \rangle_s = \langle \psi_0 | U_s^\dagger(t, t_0) o_{\mathbf{R}}^I(t) U_s(t, t_0) | \psi_0 \rangle. \quad (4)$$

Unless stated otherwise, expectation values are from now on taken with respect to the ground state  $|\psi_0\rangle$ . By ex-

panding the propagator to *linear* order in the perturbation  $H_s$ , the change in expectation value of Eq. (4) up to a final time  $T$  is given by the Kubo formula [29]

$$\Delta \langle o_{\mathbf{R}}(T) \rangle_s = i \int_{-\infty}^T \langle [H_s^I(t'), o_{\mathbf{R}}^I(T)] \rangle dt', \quad (5)$$

where  $\Delta \langle o_{\mathbf{R}}(T) \rangle_s = \langle o_{\mathbf{R}}(T) \rangle_s - \langle o_{\mathbf{R}} \rangle$  denotes the difference between the perturbed and unperturbed expectation values and we introduced the usual commutator  $[A, B] = AB - BA$ . The integral is extended to  $t_0 \rightarrow -\infty$ , assuming that the perturbation is simply turned off in the distant past. Eq. (5) fulfills causality, as any change in the expectation value of the observable at time  $T$  can only be induced by a perturbation applied at a time  $t' < T$ . Additionally, if the observable  $o_{\mathbf{R}}$  is normal ordered with respect to the ground-state  $|\psi_0\rangle$ , implying that  $\langle o_{\mathbf{R}} \rangle = 0$ , the first-order fluctuations from Eq. (5) simply correspond to the time-evolved expectation value  $\Delta \langle o_{\mathbf{R}}(T) \rangle_s = \langle o_{\mathbf{R}}(T) \rangle_s$ . Using Eq. (2), Eq. (5) can then be rewritten as

$$\langle o_{\mathbf{R}}(T) \rangle_s = \int d\mathbf{r}' \int_{-\infty}^T \mathcal{G}(\mathbf{R}, \mathbf{r}', T, t') s(\mathbf{r}', t') dt', \quad (6)$$

where

$$\mathcal{G}(\mathbf{R}, \mathbf{r}', T, t') = -i\Theta(T - t') \langle [o_{\mathbf{R}}^I(T), o_{\mathbf{r}'}^I(t')] \rangle \quad (7)$$

is a generalized susceptibility, with the step function  $\Theta(T - t')$  explicitly enforcing causality. This object can be directly identified with the Retarded Green's Function (RGF) of the observable, an essential quantity that characterizes the system's causal response to external perturbations and provides key information about its dynamical and spectral behavior. Interestingly, Eq. (6) also shows that the latter can be expressed as the functional derivative

$$\mathcal{G}(\mathbf{R}, \mathbf{r}', T, t') = \left. \frac{\delta \langle o_{\mathbf{R}}(T) \rangle_s}{\delta s(\mathbf{r}', t')} \right|_{s=0}. \quad (8)$$

As shown in the next Section, this formulation provides the basis for the development of several quantum algorithms to compute the RGF.

## III. METHODS

To make use of Eq. (8) for the calculation of the RGFs on a digital quantum computer, we first need to determine how the relevant functional derivatives can be computed with one or more quantum circuits. The working assumption is that a quantum register can be initialized in the ground state  $|\psi_0\rangle$  and that both the unperturbed and perturbed propagators can be efficiently implemented – e.g., via a product formula – in a digital quantum simulation. Moving back to the Schrödinger picture, we also assume that – in the spirit of a Suzuki-Trotter decomposition – the action of  $H_0$  and  $H_s(t')$  can

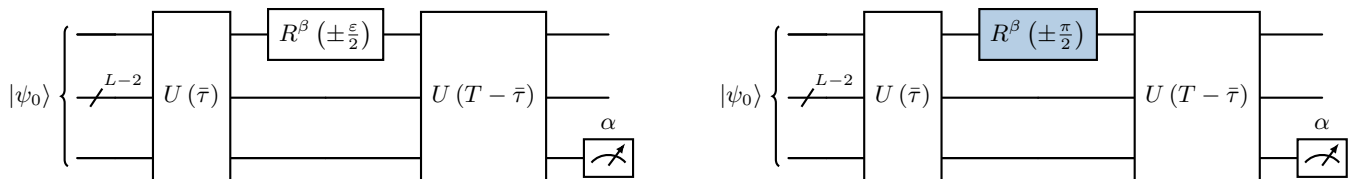


FIG. 1. **Circuit schemes for the finite differences and local circuit perturbation approaches.** Circuit to compute the RGF as in Eq. (8) between the first and last site with a single (local-time) circuit perturbation  $R^\beta(\cdot)$ . The argument of the rotation gate is a small positive angle  $\pm\epsilon/2$  for the FD approach (left) and  $\pm\pi/2$  in the LCP approach (right).  $|\psi_0\rangle$  is the initial state,  $T$  the total simulation time,  $N$  the number of Trotter steps and  $\bar{\tau} = \tau(\bar{n} - 1)$ ,  $\tau = T/N$  (see also main text).  $U(\cdot)$  indicates the time evolution operator,  $U(0) \equiv \mathbb{1}^{\otimes L}$  and the quantum register is composed of  $L$  qubits.

be factorized to yield a total propagator up to time  $T$  of the form

$$U_s(T, N) = \prod_{n=0}^{N-1} \left[ e^{-iH_0\tau} e^{-iH_s(n\tau)\tau} \right], \quad (9)$$

where  $\tau = T/N$  and  $H_s$  is evaluated on a discrete set of time points. We can then construct the functional

$$\mathcal{F}[s] = \langle U_s^\dagger(T, N) o_{\mathbf{R}} U_s(T, N) \rangle, \quad (10)$$

which corresponds to the digital quantum simulation of the expectation value  $\langle o_{\mathbf{R}}(T) \rangle$  with a specific choice of the force function  $s(\mathbf{r}', t')$  across positions  $\mathbf{r}'$  and times  $t' \in [0, T]$  for a total evolution time  $T$ .

### A. Local circuit perturbation

By using a Dirac delta in both position and time as a test function, the functional derivative of  $\mathcal{F}$  with respect to  $s$  can formally be expressed as

$$\frac{\delta \mathcal{F}[s]}{\delta s} = \lim_{\epsilon \rightarrow 0} \frac{\mathcal{F}[s + \epsilon \delta(\mathbf{r}' - \mathbf{r}) \delta(t' - t)] - \mathcal{F}[s]}{\epsilon}. \quad (11)$$

Recalling from Eq. (8) that  $\mathcal{G}$  is given by the above expression evaluated around a constant null perturbation  $s = 0$ , we can approximate it via the Finite Differences (FD) expression

$$\mathcal{G}(\mathbf{R}, \mathbf{r}, T, t) \approx \left[ \langle U_{\delta s}^\dagger(T, N) o_{\mathbf{R}} U_{\delta s}(T, N) \rangle - \langle U_0^\dagger(T, N) o_{\mathbf{R}} U_0(T, N) \rangle \right] \epsilon^{-1}, \quad (12)$$

where  $\delta s = \epsilon \delta(\mathbf{r}' - \mathbf{r}) \delta(t' - t)$ ; with some abuse of notation, we identify from here on  $U_{\delta s} \equiv U_\epsilon$ . The time evolution in the first line of Eq. (12) is generated by the space- and time-local perturbation

$$H_\epsilon(t'; \mathbf{r}, t) = \epsilon \delta(t' - t) o_{\mathbf{r}}, \quad (13)$$

with  $\epsilon \ll 1$ , i.e., a small kick applied to the system at position  $\mathbf{r}$  and time  $t$ , whose parametric dependency is indicated after the semicolon. The second term of Eq. (12) is instead the ground-state expectation value

$\langle o_{\mathbf{R}} \rangle$ , which remains constant under the unperturbed evolution assuming negligible Suzuki-Trotter discretization errors. Notice that, while in Eq. (11) we used the so-called forward definition of the FD ratio, the accuracy can be improved from  $\mathcal{O}(\epsilon)$  to  $\mathcal{O}(\epsilon^2)$  by using a symmetric increment of  $\pm\epsilon/2$ . Such higher-order version (see Fig. 1) will be adopted henceforth.

To be more concrete, assume that  $o_{\mathbf{R}} = \sigma_R^\alpha$  and  $o_{\mathbf{r}} = \sigma_r^\beta$  are, for instance, single qubit Pauli operators acting on a one-dimensional spin-1/2 lattice. In a quantum circuit representation, the first term on the r.h.s. of Eq. (12) is then obtained by introducing a single-qubit rotation gate around the axis  $\beta$  on the  $r$ -th qubit at the  $\bar{n}$ -th time step (with  $t = \bar{n}\tau$ ) and measuring  $\sigma_R^\alpha$  at the final time  $T$ , see Fig. 1 (left). The second term is, as already mentioned, simply the unperturbed ground state expectation value of  $\sigma_R^\alpha$ . For  $t = 0$ , this protocol essentially corresponds to the algorithm proposed in Ref. [28] in which, similarly to an actual linear response experiment, a system is initialized in the ground state and locally driven with a small external field.

In practice, the FD method applied in Eq. (12) is highly susceptible to numerical instabilities, particularly in the context of quantum computation: in realistic scenarios, the calculation of expectation values is affected by both hardware and statistical noise. While the former can typically be addressed through error suppression and mitigation techniques [30–33], the latter often requires substantial sampling efforts to achieve sufficiently high precision for a reliable application of this approach.

Interestingly, a more robust solution is available in many concrete use cases via a targeted choice of the perturbation parameter. In fact, one may notice that the expression for  $\mathcal{G}$  in Eq. (12) is simply an approximation of the partial derivative  $\partial F / \partial \epsilon$ , evaluated at  $\epsilon = 0$ , of the function

$$F(\epsilon) = \langle U_\epsilon^\dagger(T, N) o_{\mathbf{R}} U_\epsilon(T, N) \rangle, \quad (14)$$

with

$$U_\epsilon(T, N) = e^{-iH_0[T-\bar{\tau}]} e^{-i\epsilon o_{\mathbf{r}}(\bar{n}\tau)\tau} e^{-iH_0\bar{\tau}}, \quad (15)$$

and  $\bar{\tau} = \tau(\bar{n} - 1)$ . The quantity  $F(\epsilon)$  can be directly interpreted as the output produced by an  $\epsilon$ -parametrized quantum circuit [34]. If  $H_\epsilon$  is sufficiently simple, one

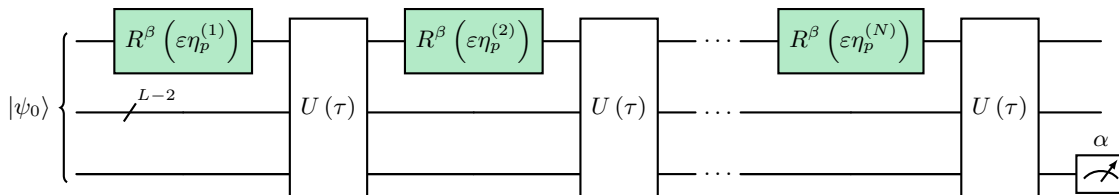


FIG. 2. **Circuit scheme for the simultaneous circuit perturbation approach.** Circuit to compute the RGF as in Eq. (8) between the first and last site with  $N$  circuit perturbations  $R^\beta(\epsilon\eta_p^{(k)})$ . Each rotation angle  $\eta_p^{(k)}$  is sampled from a Rademacher distribution of the  $N$ -dimensional random vector  $\boldsymbol{\eta}_p$ . For the notation, see also Fig. 1.

can then apply what is known as the Parameter-Shift Rule (PSR) [35, 36] to obtain an *exact* expression for  $\partial F/\partial\epsilon$  in terms of two evaluations of  $F$  on macroscopically different choices of the input. In particular, when  $U_\epsilon(\tau) = e^{-i\tau o_{\mathbf{r}}(\bar{n}\tau)\tau}$  is generated by a single-qubit Pauli operator, the finite shift values are simply  $\pm\pi/2$  and Eq. (12) is replaced by

$$\mathcal{G}(\mathbf{R}, \mathbf{r}, T, t) = 1/2 [F(\pi/2) - F(-\pi/2)] . \quad (16)$$

This approach can be formalized by demonstrating that the derivation of PSR *naturally* results in an analytical expression identical to the RGF, as we show in Appendix A. It is interesting to note that the two contributions in Eq. (16) are equal and opposite due to the symmetry in the product of the expectation values of the RGFs [27]. Consequently, flipping the sign of the angle results in a sign flip of the RGFs. A schematic description of this technique, which we will refer to as Local Circuit Perturbation (LCP) in the following, is depicted in Fig. 1 (right). Clarifying this link between derivatives and RGFs constitutes our first contribution. The LCP result, which is consistent with the derivation based on Ramsey interferometry reported in Ref. [27], can in principle be generalized to more complex  $H_\epsilon$  generators using linear combination of unitaries [36], albeit at the cost of (locally) reintroducing one ancilla. In this case the latter, unlike in the Hadamard test, only needs to be connected to the qubit(s) associated with the first perturbation and not with the final readout one(s). Since the initial state is the ground state of  $H_0$ , any temporal evolution before the perturbation at  $t$  will be trivial as long as Suzuki-Trotter discretization errors can be neglected. In practice, this allows us to remove the block  $U(\bar{\tau})$  in Fig. 1 (right), which in turn leads to shorter circuits for short times when applying LCP.

## B. Simultaneous circuit perturbation

The LCP procedure outlined above is particularly convenient, compared to standard ancilla-based quantum algorithms used to evaluate dynamical correlations, since it does not require a significant increase in circuit complexity or additional qubit-qubit connectivity (as long as the target observables are sufficiently local) with respect to

the basic digital quantum simulation of the target model. Moreover, if different sets of qubits encode for different positions  $\mathbf{R}$  (as it is the case, e.g., for spin lattice simulations), all local  $o_{\mathbf{R}}$  operators commute and can therefore be measured in parallel, thus requiring only a single circuit instance to reconstruct  $\mathcal{G}(\mathbf{R}, \mathbf{r}, T, t)$  between all possible choices of  $\mathbf{r}$  and a fixed position  $\mathbf{r}$ . However,  $t$  is fixed as the point in time at which the perturbation gate is inserted, such that multiple circuits are required to track the dynamics of the correlations. By relaxing the requirement for an analytic gradient, it is possible to devise a new algorithm that satisfies these conditions.

In particular, for fixed  $\mathbf{R}$ ,  $\mathbf{r}$  and  $T$ , the vector

$$\mathcal{G} = \begin{pmatrix} \mathcal{G}(\mathbf{R}, \mathbf{r}, T, t_1) \\ \mathcal{G}(\mathbf{R}, \mathbf{r}, T, t_2) \\ \vdots \\ \mathcal{G}(\mathbf{R}, \mathbf{r}, T, t_N) \end{pmatrix} = \begin{pmatrix} \delta\mathcal{F}[s]/\delta s(\mathbf{r}, t_1) \\ \delta\mathcal{F}[s]/\delta s(\mathbf{r}, t_2) \\ \vdots \\ \delta\mathcal{F}[s]/\delta s(\mathbf{r}, t_N) \end{pmatrix} \Big|_{s=0} , \quad (17)$$

for  $t_n = n\tau$ , is equivalent to the quantum circuit gradient

$$\mathcal{G} \equiv \nabla F(\boldsymbol{\epsilon})|_{\boldsymbol{\epsilon}=0} . \quad (18)$$

Here, we have introduced the natural generalization of the  $F(\epsilon)$  function from Eq. (14) to a  $N$ -parameter quantum circuit  $F(\boldsymbol{\epsilon}) = \langle U_{\boldsymbol{\epsilon}}^\dagger(T, N) o_{\mathbf{R}} U_{\boldsymbol{\epsilon}}(T, N) \rangle$ , where  $\boldsymbol{\epsilon} = (\epsilon_1, \dots, \epsilon_N)$  and the corresponding perturbation function is

$$\delta\mathbf{s} = \begin{pmatrix} \epsilon_1 \delta(\mathbf{r}' - \mathbf{r}) \delta(t' - t_1) \\ \vdots \\ \epsilon_p \delta(\mathbf{r}' - \mathbf{r}) \delta(t' - t_p) \end{pmatrix} \quad (19)$$

with

$$U_{\boldsymbol{\epsilon}}(T, N) = \prod_{n=0}^{N-1} e^{-iH_0\tau} e^{-i\epsilon_n\tau o_{\mathbf{r}}(n\tau)} . \quad (20)$$

Inspired by optimization methods that rely on gradient estimators, we adopt the stochastic approach underlying Simultaneous Perturbation Stochastic Approximation (SPSA) [37] to obtain, from a single circuit template and multiple randomized perturbations acting in parallel, an estimate of the whole gradient  $\nabla F(\boldsymbol{\epsilon})$ . Instead of local in time perturbations, the SPSA estimator is constructed by sampling realizations of a  $N$ -dimensional vector  $\boldsymbol{\eta} \in \{\pm 1\}^N$  uniformly at random, setting  $\boldsymbol{\epsilon} = \boldsymbol{\epsilon}\boldsymbol{\eta}$  and

measuring the expectation value of  $o_{\mathbf{r}}$  from the resulting circuit. In general, the latter can be constructed by taking  $S$  shots, meaning that the circuit is executed  $S$  times for each fixed choice of  $\boldsymbol{\eta}$ . If we denote with  $v_p^{(k)}$  the  $k$ -th element of the  $p$ -th random realization of a vector  $\mathbf{v}$ , the  $k$ -th component of the SPSSA gradient estimator constructed by sampling  $P$  perturbation directions (i.e. realizations of the  $\boldsymbol{\eta}$  vector) and using for each of those  $S$  circuit calls is given in its general form by

$$\hat{g}^{(k)} = \frac{1}{P} \sum_{p=0}^{P-1} \frac{1}{S} \sum_{s=0}^{S-1} \frac{\hat{E}_s(\boldsymbol{\theta} + \varepsilon \boldsymbol{\eta}_p) - \hat{E}_s(\boldsymbol{\theta} - \varepsilon \boldsymbol{\eta}_p)}{2\varepsilon} \eta_p^{(k)}, \quad (21)$$

where  $\hat{E}_s$  is the estimator of a target observable (or cost function value in an optimization setting) obtained from the  $s$ -th shot and with the parameter vector  $\boldsymbol{\theta}$  perturbed by  $\pm \varepsilon \boldsymbol{\eta}_p$  along the random direction  $\boldsymbol{\eta}_p$ . While  $\varepsilon$  is typically updated iteratively in optimization problems, in our case it remains fixed at a finite value  $< 1$ . Here,  $\hat{E}_s$  is an estimate of  $o_{\mathbf{r}}$ ,  $\boldsymbol{\theta} = 0$  and the total shot budget is  $S = PS$ . We refer to this parallel in time algorithm as the Simultaneous Circuit Perturbation (SCP) technique. For the simple case of single-spin perturbations, the structure of the quantum circuit is shown in Fig. 2, where unperturbed Trotter time evolution steps are interleaved with single-qubit rotations of random angles  $\varepsilon_p^{(k)} = \varepsilon \eta_p^{(k)}$ .

It is now easy to see that, for a compatible set of operators  $o_{\mathbf{R}}$ , we can simultaneously estimate  $\mathcal{G}(\mathbf{R}, \mathbf{r}, T, t)$  between a fixed pair  $(\mathbf{r}, T)$  and multiple choices of  $\mathbf{R}$  and  $t$ , all with a single circuit template and a single sampling experiment where only the perturbation vectors  $\{\boldsymbol{\eta}_p\}_{p=0}^{P-1}$  need to be randomized. Given that the Hamiltonian  $H_0$  is time-independent, the RGF depends only on the time difference between the perturbation and the response, rather than on their absolute times. The time-translational invariance allows the SCP approach to reconstruct the entire  $\mathcal{G}(\mathbf{R}, \mathbf{r}, T, T-t)$  trace using a single circuit. In contrast, the LCP method requires a separate experiment for each point on the curve, although with typically shorter evolution times.

Notably, the SCP algorithm design is well suited to leverage parametric circuit compilation techniques, as well as the high sampling rates that were recently demonstrated on, e.g., superconducting quantum processors [38]. This is particularly important in view of the fact that, as shown in Appendix B, the optimal estimator variance is obtained by using  $S = 1$ , i.e., a single shot per randomization of the perturbation vector. The same derivation also shows that the scaling of the sampling error follows the usual Monte Carlo inverse square-root law.

#### IV. APPLICATIONS

An important application of our proposed quantum algorithms is the efficient computation of the Dynamical

Structure Factor (DSF), a key quantity for investigating the dynamical properties of condensed matter systems. As mentioned earlier, all target models are assumed to exhibit time-translational invariance, i.e., their Hamiltonians are time-independent. In addition, the Hamiltonian  $H_0$  is taken to be spatially translationally invariant, implying that coupling constants and interactions are identical across all sites.

The DSF provides insight into the low-energy excitation spectrum and ground-state correlations of a medium. For a system of size  $L$ , given  $\int_{\mathcal{R},t} \equiv \sum_{\mathbf{R},\mathbf{r}} \int_{-\infty}^{\infty} dt$ , it is defined by

$$\mathcal{S}(\mathbf{q}, \omega) = \frac{1}{2\pi L} \int_{\mathcal{R},t} e^{-i\omega(T-t)} e^{-i\mathbf{q}\cdot(\mathbf{R}-\mathbf{r})} \mathcal{C}(\mathbf{R}, \mathbf{r}, T, t) dt, \quad (22)$$

i.e., as the Fourier transform in both space and time of dynamical correlation functions of the form

$$\mathcal{C}(\mathbf{R}, \mathbf{r}, T, t) = \langle o_{\mathbf{R}}(T) o_{\mathbf{r}}(t) \rangle. \quad (23)$$

The DSF can be easily measured, for instance, in inelastic neutron scattering experiments, and thus represents a direct link between theoretical models and experimental observations. However, computing the DSF for many body quantum systems using classical simulation techniques is, in general, a very demanding task. In fact, it has been shown that even approximate estimates of the DSF for arbitrary local Hamiltonians are BQP-hard to construct [27], thus making the DSF an ideal target of both digital and analog quantum simulation protocols [16, 17, 39]. Whenever the system is in thermal equilibrium at inverse temperature  $\beta$  and LRT applies, the DSF can be expressed in terms of the imaginary part of the RGF via the fluctuation-dissipation theorem [40, 41], namely

$$\mathcal{S}(\mathbf{q}, \omega) = [2n(\omega) \pm 1] \Im[\mathcal{G}(\mathbf{q}, \omega)]. \quad (24)$$

Here,  $n(\omega) = (e^{\beta\omega} \mp 1)^{-1}$  is the Bose-Einstein (Fermi-Dirac) distribution function and  $\mathcal{G}(\mathbf{q}, \omega)$  is the Fourier transform (in time and space) of  $\mathcal{G}(\mathbf{r}, \mathbf{r}', t, t')$ . This relation formalizes the intuitive idea that if a system's susceptibility to external changes is large, its fluctuations around equilibrium will be equally large. In fact, the imaginary part of the response function constitutes a measure of the rate of energy dissipation in the system.

##### A. Heisenberg spin-1/2 model

As a first target, we consider the one-dimensional Heisenberg model, consisting of a chain of  $L$  spin-1/2 systems coupled via nearest-neighbor exchange interactions

$$H = \sum_{r=0}^{L-1} \sum_{\alpha=x,y,z} J_r^\alpha \sigma_r^\alpha \sigma_{r+1}^\alpha, \quad (25)$$

where the  $\sigma^\alpha$  are Pauli operators and  $J_r^\alpha$  is the coupling strength between lattice sites  $r$  and  $r+1$  along the spin axis  $\alpha$  (set for our simulations uniformly to  $J = 1$ ),  $\sigma_{L+1}^\alpha = \sigma_0^\alpha$ . Furthermore, to approximate the unitary dynamics we employ a first-order Trotter decomposition, which factorizes the time evolution operator into a sequence of two-qubit gates of the form

$$e^{-iH\tau} = \prod_{\alpha=x,y,z} \prod_{r=0}^{L-1} e^{-iJ_r^\alpha \sigma_r^\alpha \sigma_{r+1}^\alpha \tau} + \mathcal{O}(\tau^2) . \quad (26)$$

For the Heisenberg model, the definition of the RGF specializes to

$$\mathcal{G}^{\alpha\beta}(R, T) = -\frac{i}{2} \Theta(T) \left\langle \left[ \sigma_R^\alpha(T), \sigma_0^\beta(0) \right] \right\rangle , \quad (27)$$

where we have set  $o_r \equiv \sigma_r^\alpha$  and, leveraging both spatial and temporal translational invariance, we have chosen the site  $r = 1$  and time  $t = 0$  as a reference. It is also easy to show that, when using spin operators (which are Hermitian), the RGF is equal to the imaginary part of the corresponding dynamical correlation function

$$\mathcal{G}^{\alpha\beta}(R, T) = \Im [\mathcal{C}^{\alpha\beta}(R, T)] = \Im \left[ \left\langle \sigma_R^\alpha(T) \sigma_0^\beta(0) \right\rangle \right] . \quad (28)$$

By expanding  $\mathcal{C}^{\alpha\beta}(r, t)$  on a basis of Hamiltonian eigenvectors  $|e\rangle$  with corresponding eigenfrequencies  $\omega_e$ , we get

$$\begin{aligned} \mathcal{C}^{\alpha\beta}(r, t) &= \sum_e \langle \psi_0 | \sigma_r^\alpha | e \rangle \langle e | \sigma_0^\beta | \psi_0 \rangle e^{-i\omega_e t} \\ &= \sum_e [a_{r,e}^{\alpha\beta} + i b_{r,e}^{\alpha\beta}] e^{-i\omega_e t} \\ &= \sum_e [a_{r,e}^{\alpha\beta} \cos \omega_e t + b_{r,e}^{\alpha\beta} \sin \omega_e t] \\ &+ i \sum_e [b_{r,e}^{\alpha\beta} \cos \omega_e t - a_{r,e}^{\alpha\beta} \sin \omega_e t] , \quad (29) \end{aligned}$$

where  $a_{r,e}^{\alpha\beta}$  ( $b_{r,e}^{\alpha\beta}$ ) are the real (imaginary) parts of the overlap coefficient  $\langle \psi_0 | \sigma_r^\alpha | e \rangle \langle e | \sigma_0^\beta | \psi_0 \rangle$ . Since the eigenvectors of the Heisenberg model are real, we can a priori set  $b_{r,e}^{\alpha\beta} = 0$  for any combination of indices [16]. We therefore conclude, using Eq. (28), that the desired RGF consists only of sinusoidal (i.e., odd) terms,

$$\mathcal{G}^{\alpha\beta}(r, t) = \sum_e a_{r,e}^{\alpha\beta} \sin \omega_e t , \quad (30)$$

whose Fourier transform in time is then purely imaginary

$$\mathcal{F}_t(\text{Eq. (30)}) \propto i\pi \sum_e a_{r,e}^{\alpha\beta} \delta(\omega - \omega_e) , \quad (31)$$

where we have selected the term with physical (positive) energies  $\omega_e \geq 0$ . Finally, taking the Fourier transform in space introduces an oscillatory factor, and by applying Eq. (24) and extracting the imaginary part, we find that

only the even terms in  $r$  survive, so that the DSF can be expressed as

$$\mathcal{S}^{\alpha\beta}(q, \omega) = \sum_{r,e} a_{r,e}^{\alpha\beta} \cos(qr) \delta(\omega - \omega_e) \quad (32)$$

up to Fourier normalization factors. Eq. (32) is reminiscent of the Lehmann representation of the DSF and constitutes the expression we will use to practically compute  $\mathcal{S}^{\alpha\beta}(q, \omega)$  for the numerical simulations in Section V.

## B. Fermi-Hubbard model

We now expand our analysis to include fermionic systems. As a test bench, we employ the Fermi-Hubbard model independently introduced in [42–44], describing interacting fermions on a lattice via the Hamiltonian

$$H = -J \sum_{\sigma, \langle \mu \nu \rangle} (a_{\sigma, \mu}^\dagger a_{\sigma, \nu} + a_{\sigma, \nu}^\dagger a_{\sigma, \mu}) + U \sum_{\mu} n_{\alpha, \mu} n_{\beta, \mu} , \quad (33)$$

where  $J$  and  $U$  are respectively the competing kinetic energy (hopping) and on-site Coulomb repulsion coefficients and the sums run over both spin species  $\alpha, \beta$  and nearest-neighbor sites  $\mu, \nu$ .

For fermionic systems, the formalism introduced in Section III becomes necessarily more involved. Following the same idea as in the linear response setting, one may add to the Hamiltonian a perturbation

$$H_s = \int d\mathbf{r}' (s_1(\mathbf{r}', t') a_{\mathbf{r}'} + s_2(\mathbf{r}', t') a_{\mathbf{r}'}^\dagger) , \quad (34)$$

where the usual creation and annihilation operators at position  $\mathbf{r}'$ ,  $a_{\mathbf{r}'}^\dagger$  and  $a_{\mathbf{r}'}$  are introduced. In second quantization, this term can either inject a particle at position  $\mathbf{r}'$  or remove one from that same position. In order for Eq. (34) to be part of a Hamiltonian, it must have a well-defined classical limit,  $\hbar \rightarrow 0$ , where the local Hamiltonian terms effectively commute at large distances and do not introduce non-commuting behavior over long ranges [45]. However, if  $s_1$  and  $s_2$  are ordinary commuting fields, the creation and annihilation operators fail to commute, regardless of the distance. This issue can be resolved by promoting  $s_1$  and  $s_2$  to Grassmann variables, which anti-commute. This translates into an anti-commutator (rather than a commutator) in the fermionic RGF expression,

$$\mathcal{G}(\mathbf{R}, \mathbf{r}, T, t) = -i\Theta(T-t) \langle \{ a_{\mathbf{R}}(T), a_{\mathbf{r}}^\dagger(t) \} \rangle , \quad (35)$$

with  $\{A, B\} = AB + BA$ . However, the protocol described in Section III is only capable of computing commutators and thus requires adaptation. A possible approach is suggested by the auxiliary operator method used in Ref. [28] which makes the problem of calculating the anti-commutator in Eq. (35) equivalent to that of calculating the commutator

$$\mathcal{G}(\mathbf{R}, \mathbf{r}, T, t) = \frac{i}{\lambda} \Theta(T-t) \langle [ \mathcal{P} a_{\mathbf{R}}(T), a_{\mathbf{r}}^\dagger(t) ] \rangle , \quad (36)$$

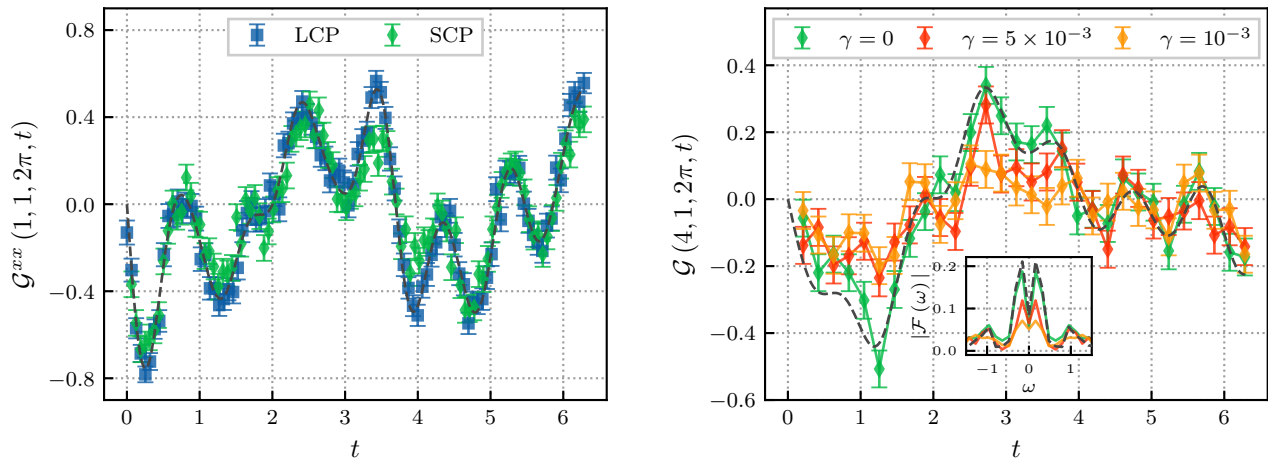


FIG. 3. **Comparison of the dynamics generated by local and simultaneous circuit perturbation.** *Left.* Bosonic Green's function as in Eq. (7) for a 10-spin Heisenberg ring,  $\alpha = \beta = x$ . The expected dynamics with  $N = 100$  Trotter steps (in the dashed dark gray line) is compared against the results produced with both the circuits in Fig. 1 (LCP) and Fig. 2 (SCP). The same shot budget is evenly distributed across each point of the LCP curve, whereas the entire budget is allocated for SCP. *Right.* Fermionic Green's function as in Eq. (35) for a 4-site 1D periodic Hubbard model,  $J = 1$  and  $U = 5$ . The expected dynamics with  $N = 30$  Trotter steps is compared with the SCP method at different values of the depolarizing parameter  $\gamma$ . The inset shows the Fourier transform of the dynamics (amplitude vs. frequency), with decreasing peaks for larger noise values. For both simulations,  $T = 2\pi$  and error bars indicate one standard deviation. For details on their calculation, see also Fig. 4.

where  $\mathcal{P}$  is a time-independent operator for which it holds  $\mathcal{P}|\psi_0\rangle = \lambda|\psi_0\rangle$  and  $\{a^\dagger(t), \mathcal{P}\} = 0 \forall t$ . As noted in Ref. [28], these assumptions are satisfied, for parity-conserving Hamiltonians, by the parity operator.

The final step involves the mapping of the operators to qubits, for which we make use of the Jordan-Wigner (JW) transformation [46], that for creation and annihilation operators yields

$$a_r^\dagger = \mathcal{Z}_r \frac{\sigma_r^x + i\sigma_r^y}{2} \quad a_r = \mathcal{Z}_r \frac{\sigma_r^x - i\sigma_r^y}{2}, \quad (37)$$

where we have denoted with  $\mathcal{Z}_r = \prod_{j < r} \sigma_j^z$  the attached JW-strings. Note that both operators in Eq. (37) anti-commute with the parity operator  $\mathcal{P} = Z_0 \dots Z_{2L-1}$ , where the factor of 2 takes care of the possibility of having different spin species. In practice then, two quantum circuits with distinct  $\mathcal{Z}_r \sigma_r^{x/y}$  perturbations are therefore required for the measurement of the RGF. With these adjustments, both the LCP and SCP protocols can be employed in the fermionic case, albeit with a perturbation that depending on the chosen fermion to qubit mapping typically remains local in time but non-local in space (see Fig. 8 (left) in Appendix D). Due to the non-local nature of the operators involved, parallel measurements – unlike in the bosonic case – are not feasible in this scenario; however, the sampling advantage offered by SCP remains valid.

In the next section we present results for both these model Hamiltonians.

## V. RESULTS

The simulations, where not otherwise specified, only considered statistical (or *shot*) noise. We adopt natural units by setting the coupling and hopping parameter to  $J_r^\alpha = J \equiv 1$ . All energies are thus expressed in units of  $J$ , and time is measured in units of  $1/J$ .

To illustrate the practical use our proposed quantum algorithms, we show the calculation of  $\mathcal{G}^{\alpha\beta}(r, t)$  with  $r = 1$  for the Heisenberg model of Section IV A on 10 spins for  $N = 100$  in Fig. 3 (left). The reported data, collected via numerical simulations, compare the exact dynamics obtained through direct matrix multiplication of the Trotter evolution with the results obtained from a simulation of the quantum circuits for LCP and SCP.

We use a total budget of  $\mathcal{S} = 2^{14}$  shots: in the case of LCP, this is divided equally across the 100 data points reported in the plot. For SCP, instead, we distribute  $\mathcal{S}$  across  $P$  independent perturbations  $\{\eta_p\}_{p=0}^{P-1}$  as described in Eq. (21). As shown in Appendix B, the variance of the  $k$ -th gradient component averaged over these perturbations when using  $\mathcal{S}$  shots each can be expressed as

$$\text{var}_{\eta, \hat{E}} [\hat{g}^{(k)}] = \frac{\text{var}_{\eta} [g^{(k)}]}{P} + \frac{c_{\text{SCP}}}{P\mathcal{S}\epsilon^2}, \quad (38)$$

where  $c_{\text{SCP}}$  is a constant. In Eq. (38), following the law of total variance, the first term originates from the variability induced by the perturbations  $\eta_p$ . The second term on the other hand represents the sampling noise associated with the operator averaging procedure required

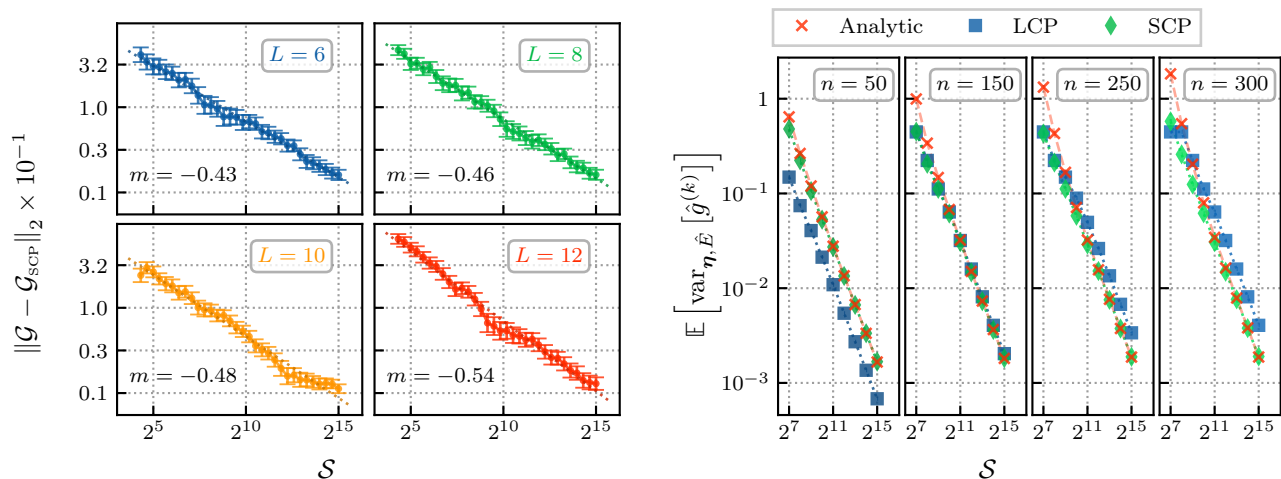


FIG. 4. **Convergence to ground truth and variance scaling.** *Left.* Scaling with the number of shots of the norm of differences between the expected dynamics and SCP in log-log scale, for an increasing number of spins. As expected, convergence occurs with scaling equal to the inverse of the root of the samples,  $\mathcal{O}(1/\sqrt{S})$ . The slopes  $m$  of the fit lines are indicated in the lower left corners, and are in good qualitative agreement with the expected value of  $-1/2$ . *Right.* Comparison of the mean of the variance estimates of the gradient in log-log scale of the LCP and SCP methods as a function of the number of shots. The red curve shows Eq. (38) for which the second term has been saturated setting  $c_{\text{SCP}} = 1$  (see also Appendix B).

to reconstruct the output (i.e., the  $\hat{E}_s(\pm\varepsilon\eta_p)$  terms of Eq. (21)) of each fixed circuit configuration. From a statistical point of view, the optimal shot allocation policy is then to choose  $S = 1$ , i.e. to change  $\{\eta_p\}_{p=0}^{P-1}$  at each shot. As already mentioned, this option may be quite demanding in practice, as it could lead to high circuit compilation and experimental control overheads in real devices unless, e.g. some form of parametric execution is available [38]. For this reason, we always assume a generic  $S \geq 1$  in all our formal derivations, although we adopt the  $S = 1$  strategy in all numerical simulations.

Notice that both LCP and SCP require two circuit evaluations per data point or gradient estimate. In the case of LCP, as described in Section III A, we reconstruct  $F(\pi/2)$  and  $F(-\pi/2)$  separately, using the full shot budget assigned to each individual time point for each evaluation. Similarly, for SCP, Eq. (21) and Eq. (38) assume that  $\hat{E}_s(\varepsilon\eta_p)$  and  $\hat{E}_s(-\varepsilon\eta_p)$  are estimated independently. In our implementation, we take  $S = 1$ , meaning that each of the two required evaluations for a given perturbation is performed with a single shot. Thus, in both cases, the total number of circuit runs is  $2S$ , with  $S$  independent perturbations available for SCP.

In Fig. 3 (right) we show a similar plot, this time for the time evolution of a 4-site 1D periodic Hubbard model, with  $J = 1$ ,  $U = 5$  (see Eq. (33)) and  $N = 30$ . On top of the comparison with the expected and Trotter dynamics for the SCP method, we also show the curves obtained by applying a depolarizing noise channel

$$\mathcal{D}_\gamma(\rho) = (1 - \gamma)\rho + \gamma \text{Tr}[\rho] \frac{\mathbb{1}}{2^L}, \quad (39)$$

where  $\gamma$  is the depolarizing error parameter,  $0 \leq \gamma \leq$

$4^L / (4^L - 1)$ . We apply the channel to all two-qubit circuit gates for increasing values of  $\gamma = 5 \cdot 10^{-3}$  and  $\gamma = 10^{-3}$ , which are in the range of typical experiments. The inset shows the (symmetric) Fourier transform of the signal: SCP demonstrates good resilience to the noise model, with frequencies that remain well recognizable for all values of  $\gamma$ . Fig. 4 (left) numerically confirms that the SCP estimates converge to the expected result with a scaling of the residual errors proportional to  $1/\sqrt{S}$ . Furthermore, for local single-qubit operators such as the ones appearing in the Heisenberg chain, the errors do not significantly scale with system size.

The potential advantages of SCP over LCP in terms of overall sampling costs are showcased in Fig. 4 (right), where we report the average variance of the gradient's estimates for the Heisenberg model as a function of the total shot budget  $S$  and for a different number of points (and thus perturbations  $N$ ) along the time axis, indicated by the figure above each line. As the mesh becomes finer, one can easily see that the errors at fixed  $S$  substantially increase for LCP, where each additional point requires a separate experiment and consumes a definite fraction of the total shots  $s_r = \lceil S/N \rceil$ . Such increase is slower for SCP, with a crossover around  $N \approx 150$ . This suggests that SCP might become particularly convenient in practical regimes of interest, where long simulation times and dense curve samplings are required to resolve higher frequencies. Since the observable is taken from the set  $\{\sigma_r^\alpha\}_{r \in [0 \dots L-1]}$ , the variance for LCP is given, according to its definition, as  $(1 - \langle \sigma_r^\alpha \rangle)^2 / N$ . Notice that here the number of Trotter steps increases with the number of perturbations, even though the total simulation time is kept fixed for all curves. Our numerical estimates are

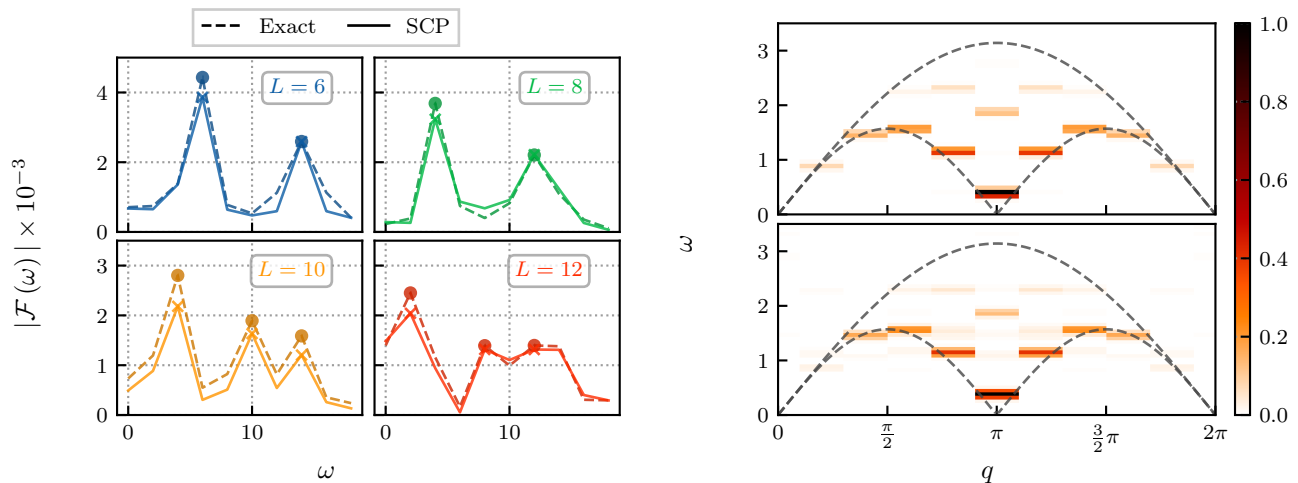


FIG. 5. **Fourier transform and dynamical structure factor.** *Left.* Fourier transform of the exact and SCP curves for an increasing number of spins. *Right.* Dynamical spin structure factor for a 10-site spin chain using exact diagonalization and SCP (top and bottom panel respectively). The dashed lines show the lower and upper limits of the two-spinon contributions as given in [47], excitations that carry most of the total intensity of the DSF [48]. The energies have been rescaled by a factor  $2\pi/\max(\omega_e)$ ; values have been normalized to 1 for comparison, and the delta-functions in Eq. (32) have been replaced by normalized Gaussians with  $\sigma = 0.2J$ .

confirmed by the analytic results obtained by a direct application of Eq. (38).

Finally, in Fig. 5 we report the frequency domain Fourier transforms of the generalized susceptibilities for Heisenberg chains of various lengths computed via SCP (left), and the calculation of the DSF for the 10-spin case (right). The RGFs utilized for the calculation of the latter are depicted in Fig. 6. Each time trace is fitted using the Fourier form introduced in Eq. (30), with the additional constraint that  $\mathcal{G}^{\alpha\alpha}(r, 0) = 0 \forall r$ , as the equal time commutator  $[\sigma_r^\alpha(0), \sigma_0^\alpha(0)]$  between any pair of local spin operators along the same axis vanishes. Notably, the use of SCP allows us to retrieve all data points along the time traces – which are required to carry out the temporal Fourier analysis and extract the  $a_{r,e}^{\alpha\beta}$  coefficients and the frequencies  $\omega_e$  – with a single circuit instance equipped with random single-qubit perturbations. Furthermore, for any choice of  $\alpha, \beta$  and  $t$ , all RGFs  $\{\mathcal{G}^{\alpha\beta}(r, t)\}_{r \in [0 \dots L-1]}$  can be computed in parallel by measuring commuting local Pauli operators. Altogether, these approaches considerably reduce the number of independent circuit templates that must be executed to carry out the spatial and temporal Fourier transform leading to  $\mathcal{S}^{\alpha\beta}(q, \omega)$  via Eq. (32). Within finite-size effects, our results are consistent with those obtained using variational Monte Carlo [47], restricted Boltzmann machines [49] or a Bethe *Ansatz* approach [50].

## VI. CONCLUSIONS

In this work, we presented a novel sample-based, ancilla-free algorithm to compute dynamical correlations and Green’s functions on quantum computers. Our

method represents a randomized, parallel alternative to standard linear-response inspired ones and can produce denser time traces at reduced sampling costs compared to local, sequential procedures.

From a practical perspective, our techniques are particularly well suited to benefit from parametric compilation tools and the high repetition rates available on state-of-the-art quantum processors based on superconducting technology. Our approach also lends itself to the application of recent developments that aim to denoise and extend response functions thanks to their positive-definiteness [51]. At the same time, our analytical treatment highlighted a systematic connection between response functions and quantum circuit derivatives which might be leveraged for further theoretical and computational developments. In the longer term, the idea of computing temporal properties of quantum systems in parallel might be further extended by using proper clock qubit registers [52].

We demonstrated the validity of our approach with extensive numerical simulations, finding good agreement between the proposed LCP and SCP protocols and the expected results. In particular, we implemented a robust and inexpensive workflow to compute dynamical structure factors and Fourier spectra for spin and fermionic models on lattice, thus confirming that spectroscopic analyses constitute an excellent test bed for current and future quantum computers.

## ACKNOWLEDGMENTS

We thank Julien Gacon and Matthias Lehmkuhler for useful discussions, and Anthony Gandon for valuable

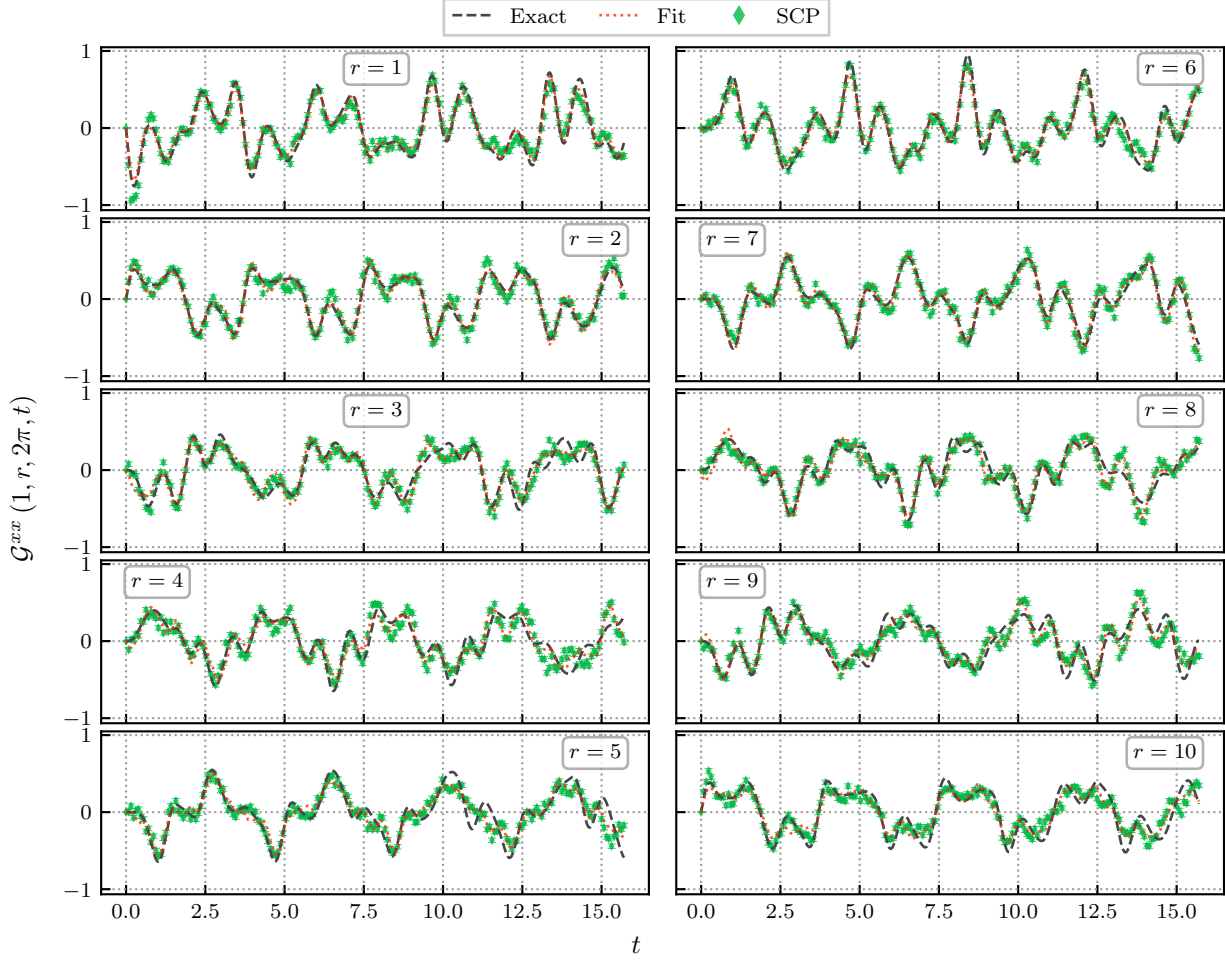


FIG. 6. **Green's functions and fits for the calculation of dynamical structure factor.** Green's functions as in Eq. (27) for a 10-qubit chain for  $r \in \{0, \dots, 9\}$ , using  $S = 2^{16}$  shots. The fits (black curves) are performed using *iminuit* [53]. Note how all the green curves are obtained by running a single, non-parametrized circuit.

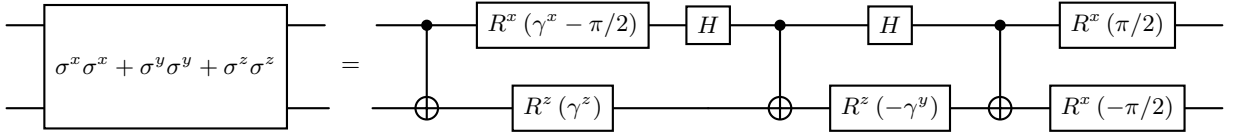


FIG. 7. **Heisenberg circuit decomposition.** 3-CNOT circuit decomposition for the digital quantum simulation of the 2-qubit Heisenberg model. For each single-qubit rotation  $R^\alpha(\cdot)$ , we define the angle as  $\gamma^\alpha = 2J^\alpha \tau$ , where  $\tau = T/N$  is the elementary time step,  $T$  the total simulation time window and  $N$  is the number of Trotter steps. The phase difference from the expected unitary is of  $e^{i\pi/4}$ .

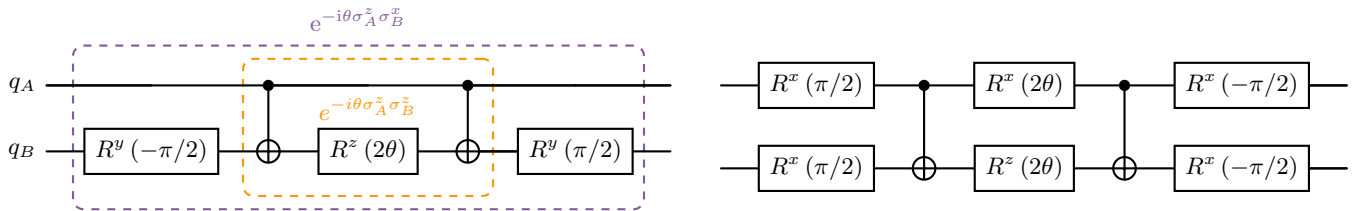


FIG. 8. **Fermi-Hubbard circuit decomposition.** *Left.* Circuit decomposition for implementing the exponential of  $\sigma^z \sigma^z$  (yellow rectangle) and  $\sigma^z \sigma^x$  (purple rectangle). The case  $\sigma^z \sigma^y$  is obtained by flipping the sign of the angles of both  $R^y$  rotations and substituting  $R^y \rightarrow R^x$ . *Right.* 2-CNOT circuit decomposition of the  $\sigma^x \sigma^x + \sigma^y \sigma^y$  exponential implementing the JW-transformed hopping term (see Eqs. (33) and (37)).

feedback on the manuscript. Plot colors are adapted from *SciencePlots* [54]. This research was supported by NCCR MARVEL, a National Center of Competence in Research, funded by the Swiss National Science Foundation (grant number 205602) and by RESQUE funded by the Swiss National Science Foundation (grant number 225229).

### Appendix A: Calculation of the retarded Green's function and parameter-shift rule

In this paragraph we show that the analytical form of the PSR in the case of a Pauli gate *exactly* matches the one in Eq. (7), thus establishing a link between the calculation of a derivative of a parametrized Pauli rotation and the calculation of the RGF. We start by considering a parametrized gate in the form

$$U_\ell(\theta_\ell) = \exp\left(-i\frac{\theta_\ell}{2}P\right), \quad (\text{A1})$$

with  $P$  a Pauli operator. Let us examine the action of Eq. (A1) in a parametrized quantum circuit, where the overall unitary transformation can be expressed as a product of  $N$  unitaries,

$$U(\boldsymbol{\theta}) = \prod_{\ell=0}^{N-1} U_\ell(\theta_\ell). \quad (\text{A2})$$

Without loss of generality – since any Hermitian operator can be expanded as a linear combination of Pauli operators – we may write a generic observable as  $Q$ , another Pauli operator. The action of the quantum circuit on  $Q$  can be expressed by the function

$$\mathcal{U}(\boldsymbol{\theta}) = \left\langle \psi_{\ell-1} \left| U_\ell^\dagger(\theta_\ell) Q U_{\ell+1} U_\ell(\theta_\ell) \right| \psi_{\ell-1} \right\rangle, \quad (\text{A3})$$

where we have absorbed any gate happening before the  $\ell$ -th gate in the initial state,  $|\psi_{\ell-1}\rangle = \prod_{j=0}^{\ell-1} U_j(\theta_j) |\psi_0\rangle$  and any gate applied after in the observable  $Q_{\ell+1} = \prod_{j=N-1}^{\ell+1} U_j^\dagger(\theta_j) Q \prod_{j=\ell+1}^{N-1} U_j(\theta_j)$ . Since the function in Eq. (A3) depends smoothly on the parameter  $\theta_\ell$ , it admits a well-defined gradient,

$$\nabla_{\theta_\ell} \mathcal{U}(\boldsymbol{\theta}) = -\frac{i}{2} \left\langle \psi_{\ell-1} \left| U_\ell^\dagger(\theta_\ell) [Q_{\ell+1}, P] U_\ell(\theta_\ell) \right| \psi_{\ell-1} \right\rangle, \quad (\text{A4})$$

which follows from the derivative

$$\nabla_{\theta_\ell} U_\ell(\theta_\ell) = -\frac{i}{2} U_\ell(\theta_\ell) P. \quad (\text{A5})$$

For commutators involving Pauli operators, one can use the identity introduced in Ref. [35]

$$[Q, P] = i \left( U_\ell^\dagger\left(\frac{\pi}{2}\right) Q U_\ell\left(\frac{\pi}{2}\right) - U_\ell^\dagger\left(-\frac{\pi}{2}\right) Q U_\ell\left(-\frac{\pi}{2}\right) \right), \quad (\text{A6})$$

Substituting this into Eq. (A4) yields the PSR,

$$\nabla_{\theta_\ell} \mathcal{U}(\boldsymbol{\theta}) = \frac{1}{2} \left[ \mathcal{U}\left(\theta_\ell + \frac{\pi}{2}\right) - \mathcal{U}\left(\theta_\ell - \frac{\pi}{2}\right) \right]. \quad (\text{A7})$$

For our purposes, however, it is sufficient to stop at Eq. (A4). Focusing on the first term of the commutator and ignoring for a moment the prefactor of  $-i/2$ , by expanding back the gates in the state and the observable we get

$$\left\langle \psi_0 \left| \prod_{j=N-1}^0 U_j^\dagger Q \prod_{j=\ell+1}^{N-1} U_j P U_\ell \prod_{j=0}^{\ell-1} U_j \right| \psi_0 \right\rangle, \quad (\text{A8})$$

where we removed the  $\theta$  dependency from the unitaries for ease of notation. We can now insert an identity  $\prod_{j=0}^\ell U_j \prod_{j=i}^0 U_j^\dagger$  before  $P$ , yielding

$$\left\langle \psi_0 \left| \prod_{j=N-1}^0 U_j^\dagger Q \prod_{j=0}^{N-1} U_j \prod_{j=i}^0 U_j^\dagger P \prod_{j=0}^\ell U_j \right| \psi_0 \right\rangle. \quad (\text{A9})$$

With Fig. 1 in mind, the unitaries can be identified as  $N$  Trotter blocks with  $\theta \equiv \tau = T/N$ , where  $T$  is the total evolution time. The Paulis in Eq. (A9) are thus evolved to times  $Q(T)$  and  $P(t')$  respectively, with  $t' = \ell\tau$ . Since the second commutator term in Eq. (A4) produces the complex conjugate of Eq. (A9), we finally come to

$$\text{Eq. (A4)} = -\frac{i}{2} \langle \psi_0 | [Q(T), P(t')] | \psi_0 \rangle. \quad (\text{A10})$$

This expression corresponds to Eq. (7) up to a factor of 2, which, as mentioned in the main text, takes into account the symmetries of the RGFs. This final observation marks the connection between the PSR and the RGF.

### Appendix B: Variance of the simultaneous circuit perturbation gradient

The variance of each component  $\hat{g}^{(k)}$ , with  $k \in \{0, \dots, N-1\}$  of the SCP gradient estimator defined in Eq. (21) with respect to both the shot and circuit perturbation randomness (that is, the variance of each of the  $N$  elements in the  $P$  instances) can be computed starting from the law of total variance,

$$\begin{aligned} \text{var}_{\boldsymbol{\eta}, \hat{E}} \left[ \hat{g}^{(k)} \right] &= \text{var}_{\boldsymbol{\eta}} \left[ \mathbb{E}_E \left[ \hat{g}^{(k)} | \boldsymbol{\eta}_1, \dots, \boldsymbol{\eta}_p \right] \right] + \\ &+ \mathbb{E}_{\boldsymbol{\eta}} \left[ \text{var}_E \left[ \hat{g}^{(k)} | \boldsymbol{\eta}_1, \dots, \boldsymbol{\eta}_p \right] \right]. \end{aligned}$$

Using the linearity of the expectation value, with  $\mathbb{E} \left[ \hat{E}_s \right] \equiv E_s$  and by introducing the notation  $\hat{E}_{s,p}^\pm = \hat{E}_s(\theta \pm \boldsymbol{\eta}_p \varepsilon)$ , this can be rewritten as

$$\begin{aligned} \text{var}_{\boldsymbol{\eta}} \left[ \frac{1}{P} \sum_{p=0}^{P-1} \frac{E(\theta + \boldsymbol{\eta}_p \varepsilon) - E(\theta - \boldsymbol{\eta}_p \varepsilon)}{2\varepsilon} \boldsymbol{\eta}_p^{(k)} \right] &+ \quad (\text{B1}) \\ + \mathbb{E}_{\boldsymbol{\eta}} \left[ \frac{1}{(PS2\varepsilon)^2} \text{var}_E \left[ \sum_{p=0}^{P-1} \sum_{s=0}^{S-1} \left( \hat{E}_{s,p}^+ - \hat{E}_{s,p}^- \right) \boldsymbol{\eta}_p^{(k)} \right] \right] & \quad (\text{B2}) \end{aligned}$$

Given that  $\text{var}_{\boldsymbol{\eta}} [g^{(k)}]$  is the same over i.i.d. different realizations of the perturbation vector  $\boldsymbol{\eta}_p$ , Eq. (B1) can

be expressed as  $N^{-1} \text{var}_{\boldsymbol{\eta}} [g^{(k)}]$ . For Eq. (B2), we start by noticing that the sums of  $\hat{E}_s^+$  and  $\hat{E}_s^-$  are not correlated,

$$\text{Eq. (B2)} = \frac{1}{(PS2\varepsilon)^2} \mathbb{E}_{\boldsymbol{\eta}} \left[ \sum_{p=0}^{P-1} \eta_p^{(k)} \left[ \text{var}_E \left( \sum_{s=0}^{S-1} \hat{E}_{s,p}^+ \right) + \text{var}_E \left( \sum_{s=0}^{S-1} \hat{E}_{s,p}^- \right) \right] \right] = \quad (\text{B3})$$

$$= \frac{1}{(PS2\varepsilon)^2} \mathbb{E}_{\boldsymbol{\eta}} \left[ \sum_{p=0}^{P-1} \eta_p^{(k)} S \left[ \nu^2 (\theta + \boldsymbol{\eta}_p \varepsilon) + \nu^2 (\theta - \boldsymbol{\eta}_p \varepsilon) \right] \right] = \frac{1}{PS\varepsilon^2} \mathbb{E}_{\boldsymbol{\eta}} \left[ \frac{\nu^2 (\theta + \boldsymbol{\eta}_1 \varepsilon) + \nu^2 (\theta - \boldsymbol{\eta}_1 \varepsilon)}{4} \eta_1^{(k)} \right], \quad (\text{B4})$$

where in the two equations Eq. (B4) we first denote by  $\nu^2$  the variance of the function computed at a point and then we fix the realization of  $\eta_p^{(k)}$  to  $\eta_1^{(k)}$ . We can identify for brevity the expectation value in Eq. (B4) as

$$c_{\text{SCP}} \equiv \mathbb{E}_{\boldsymbol{\eta}} \left[ \frac{\nu^2 (\theta + \boldsymbol{\eta}_1 \varepsilon) + \nu^2 (\theta - \boldsymbol{\eta}_1 \varepsilon)}{4} \eta_1^{(k)} \right]. \quad (\text{B5})$$

Note that in this case we cannot distribute the expectation value to the terms  $\nu^2$  and  $\eta_1^{(k)}$  separately since they are not independent variables and that  $c_{\text{SCP}}$  is upper-

bounded by 1/2. In fact,  $\nu^2 = (1 - \langle \sigma_r^\alpha \rangle)^2 / N \leq 1$ , since (as for the LCP case explained in Section V) only one Pauli is evaluated for each parameter extraction and thus, in particular, for  $\theta \pm \boldsymbol{\eta}_1 \varepsilon$ .

We can piece this together, obtaining for the variance the final expression

$$\text{var}_{\boldsymbol{\eta}, \hat{E}} [\hat{g}^{(k)}] = \frac{\text{var}_{\boldsymbol{\eta}} [g^{(k)}]}{P} + \frac{c_{\text{SCP}}}{PS\varepsilon^2}. \quad (\text{B6})$$

The variance appearing in the first term in can be expanded to first order as

$$\text{var}_{\boldsymbol{\eta}} [g^{(k)}] = \text{var}_{\boldsymbol{\eta}} \left[ \frac{E(\theta + \boldsymbol{\eta}_1 \varepsilon) - E(\theta - \boldsymbol{\eta}_1 \varepsilon)}{2\varepsilon} \eta_1^{(k)} \right] = \quad (\text{B7})$$

$$= \text{var}_{\boldsymbol{\eta}} \left[ \boldsymbol{\eta}_1^\top \nabla E(\theta) \eta_1^{(k)} \right] = \text{var}_{\boldsymbol{\eta}} \left[ \sum_{n=0}^{d-1} \frac{\partial}{\partial \theta_n} E(\theta) \eta_1^{(n)} \eta_1^{(k)} \right] = \quad (\text{B8})$$

$$= \left( \sum_{nm} \partial_n E(\theta) \partial_m E(\theta) \mathbb{E}_{\boldsymbol{\eta}} \left[ \eta_1^{(n)} \eta_1^{(m)} \right] \right) - \left( \sum_n \partial_n E(\theta) \mathbb{E}_{\boldsymbol{\eta}} \left[ \eta_1^{(n)} \eta_1^{(k)} \right] \right)^2 = \quad (\text{B9})$$

$$= \sum_n (\partial_n E(\theta))^2 - (\partial_k E(\theta))^2 = \|\nabla E\|_2^2 - (\nabla E^{(k)})^2, \quad (\text{B10})$$

where the first equivalence in Eq. (B8) is given by a first-order Taylor expansion to  $\mathcal{O}(\varepsilon^2)$  – i.e. precisely the bias in the SPSA gradient estimator  $\mathbb{E}[\hat{g}^{(k)}] = \nabla E^{(k)}$  – while in Eq. (B10) we use  $\mathbb{E}_{\boldsymbol{\eta}} [\eta_1^{(n)} \eta_1^{(m)}] = \delta_{nm}$ .

By expressing Eq. (B6) in terms of the total shot budget  $\mathcal{S} = PS$ , one observes that while the second term depends jointly on  $\mathcal{S}$  only (which we assume fixed), the first becomes linear in  $\mathcal{S}$ . This implies that the optimal shot distribution strategy is to use a single shot ( $S = 1$ ) per randomization and maximize the number of independent samples  $P$ . With this allocation, we also recover the expected asymptotic scaling noted in Section V of  $\text{var}_{\boldsymbol{\eta}} [g^{(k)}] \propto \mathcal{O}(1/\sqrt{\mathcal{S}})$ .

### Appendix C: Dynamical structure factor calculation

To compute Eq. (32) one possible approach is to fit the curves of the RGFs obtained via SCP and extract the frequencies  $\omega_e$ . To this end, we first obtain an ordered list of candidate frequencies by performing a Fourier transform on the observed data and extracting the most dominant peaks in the power spectrum. We then construct a sequence of models, each incorporating one additional frequency from this list, moving from a single-frequency model up to a predefined maximum. For each model, we employ a nonlinear least-squares minimization to fit the sine parameters (amplitudes and frequencies) appearing in Eq. (30), minimizing the overall chi-squared statistic. After fitting, we calculate the Bayesian Information Criterion (BIC) [55] for each model to balance goodness-of-fit against model complexity. The final model is cho-

sen as the one yielding the lowest BIC, thereby retaining only those frequencies that produce a statistically robust improvement in fit without excessively increasing the parameter count.

We emphasize that this is only one possible way to extract frequencies, which is not the main focus of this paper, and that more sophisticated methods exist in principle. The technique described above, with the combination of a Fourier-based warm start and iterative fitting, provides both a reasonable initialization and a systematic mechanism for pattern selection.

#### Appendix D: Circuit decomposition for the Heisenberg and Fermi-Hubbard model

The Suzuki-Trotter expansion of the Heisenberg Hamiltonian in Eq. (25) breaks the evolution into two-body blocks that can be applied in parallel on even and odd qubits. Each of these blocks, shown in Fig. 7, can be implemented with a 3-CNOT circuit [56]. The circuit perturbations, as mentioned in the main text, are in this case just one-qubit rotations implemented by single-qubit gates  $R^\alpha(\cdot)$ , with the axis of the rotation pointing in the direction of the applied perturbation.

The quantum simulation of the Fermi-Hubbard model requires the implementation of both the hopping and interaction terms in Eq. (33). After applying the JW transformation, the interaction term leads to products

of single and double Pauli  $\sigma^z$  operators. The exponentials of these terms can be implemented through single-qubit  $z$ -rotations and, in the case of two-body terms, through the circuit shown in Fig. 8 (left, yellow rectangle). The hopping term, on the other hand, gives rise - according to Eq. (37) - to Pauli strings of the form  $\mathcal{Z}\sigma^\alpha$ , with  $\alpha = x, y$ . Knowing how to build exponentials of  $\sigma^z$  strings, these terms can be realized in the circuit by applying suitable basis transformations through single-qubit rotations. Specifically, the following relations hold:

$$R^y(\pi/2)\sigma^zR^y(-\pi/2) = \sigma^x, \quad (\text{D1})$$

$$R^x(-\pi/2)\sigma^zR^x(\pi/2) = \sigma^y. \quad (\text{D2})$$

An example of this procedure is illustrated in Fig. 8 (left, purple rectangle), where the exponential of a  $\sigma^z\sigma^x$  term is implemented. This provides a representative case of a circuit perturbation in the fermionic setting, where, in the general case of correlations between distant indices, chains of CNOT gates span between the first and last qubits involved (denoted respectively  $q_A$  and  $q_B$ ), rendering the operation non-local in space while remaining local in time. Circuits implementing perturbations of the form  $\sigma^{x/y}$ , followed by measurements of the corresponding observable conjugated by the parity operator  $\mathcal{P}$  (see main text), yield an estimate of the RGF according to either the PSR or SCP approach. Finally, Fig. 8 (right) shows the two-CNOT decomposition of the full hopping term ( $\sigma^x\sigma^x + \sigma^y\sigma^y$ ).

- 
- [1] A. Miessen, P. J. Ollitrault, F. Tacchino, and I. Tavernelli, *Nature Computational Science* **3**, 25 (2022).
- [2] A. Di Meglio, K. Jansen, I. Tavernelli, C. Alexandrou, S. Arunachalam, *et al.*, *PRX Quantum* **5**, 037001 (2024).
- [3] Y. Alexeev, M. Amsler, M. A. Barroca, S. Bassini, T. Battelle, *et al.*, *Future Generation Computer Systems* **160**, 666 (2024).
- [4] Y. Kim, A. Eddins, S. Anand, K. X. Wei, E. Van Den Berg, S. Rosenblatt, H. Nayfeh, Y. Wu, M. Zaletel, K. Temme, and A. Kandala, *Nature* **618**, 500 (2023).
- [5] R. Somma, G. Ortiz, J. E. Gubernatis, E. Knill, and R. Laflamme, *Physical Review A* **65**, 042323 (2002).
- [6] R. N. Tazhigulov, S.-N. Sun, R. Haghshenas, H. Zhai, A. T. Tan, N. C. Rubin, R. Babbush, A. J. Minnich, and G. K.-L. Chan, *PRX Quantum* **3**, 040318 (2022).
- [7] J. S. Pedernales, R. Di Candia, I. L. Egusquiza, J. Casanova, and E. Solano, *Physical Review Letters* **113**, 020505 (2014).
- [8] A. Roggero and J. Carlson, *Phys. Rev. C* **100**, 034610 (2019).
- [9] F. Jamet, A. Agarwal, and I. Rungger, “Quantum subspace expansion algorithm for Green’s functions,” (2022).
- [10] P. J. Ollitrault, A. Kandala, C.-F. Chen, P. K. Barkoutsos, A. Mezzacapo, M. Pistoia, S. Sheldon, S. Woerner, J. M. Gambetta, and I. Tavernelli, *Physical Review Research* **2**, 043140 (2020).
- [11] J. Rizzo, F. Libbi, F. Tacchino, P. J. Ollitrault, N. Marzari, and I. Tavernelli, *Physical Review Research* **4**, 043011 (2022).
- [12] J. Selisko, M. Amsler, C. Wever, Y. Kawashima, G. Samsonidze, R. U. Haq, F. Tacchino, I. Tavernelli, and T. Eckl, “Dynamical Mean Field Theory for Real Materials on a Quantum Computer,” (2024).
- [13] T. E. Baker, *Physical Review A* **103**, 032404 (2021).
- [14] F. Jamet, A. Agarwal, C. Lupo, D. E. Browne, C. Weber, and I. Rungger, “Krylov variational quantum algorithm for first principles materials simulations,” (2021).
- [15] R. Irmejs and R. A. Santos, *Quantum* **9**, 1639 (2025).
- [16] A. Chiesa, F. Tacchino, M. Grossi, P. Santini, I. Tavernelli, D. Gerace, and S. Carretta, *Nature Physics* **15**, 455 (2019).
- [17] F. Tacchino, A. Chiesa, S. Carretta, and D. Gerace, *Advanced Quantum Technologies* **3**, 1900052 (2020).
- [18] M. Gärttner, J. G. Bohnet, A. Safavi-Naini, M. L. Wall, J. J. Bollinger, and A. M. Rey, *Nature Physics* **13**, 781 (2017).
- [19] A. Baroni, J. Carlson, R. Gupta, A. C. Y. Li, G. N. Perdue, and A. Roggero, *Physical Review D* **105**, 074503 (2022).
- [20] J. Braumüller, A. H. Karamlou, Y. Yanay, B. Kannan, D. Kim, M. Kjaergaard, A. Melville, B. M. Niedzielski, Y. Sung, A. Vepsäläinen, R. Winik, J. L. Yoder, T. P. Orlando, S. Gustavsson, C. Tahan, and W. D. Oliver, *Nature Physics* **18**, 172 (2022).
- [21] S.-N. Sun, M. Motta, R. N. Tazhigulov, A. T. Tan, G. K.-

- L. Chan, and A. J. Minnich, *PRX Quantum* **2**, 010317 (2021).
- [22] S. Endo, I. Kurata, and Y. O. Nakagawa, *Physical Review Research* **2**, 033281 (2020).
- [23] F. Libbi, J. Rizzo, F. Tacchino, N. Marzari, and I. Tavernelli, *Physical Review Research* **4**, 043038 (2022).
- [24] K. Huang, X. Cai, H. Li, Z.-Y. Ge, R. Hou, H. Li, T. Liu, Y. Shi, C. Chen, D. Zheng, K. Xu, Z.-B. Liu, Z. Li, H. Fan, and W.-H. Fang, *The Journal of Physical Chemistry Letters* **13**, 9114 (2022).
- [25] K. Mitarai and K. Fujii, *Physical Review Research* **1**, 013006 (2019).
- [26] M. Kastner, P. Osterholz, and C. Gross, “Ancilla-free measurement of out-of-time-ordered correlation functions: General measurement protocol and Rydberg atom implementation,” (2024).
- [27] M. L. Baez, M. Goihl, J. Haferkamp, J. Bermejo-Vega, M. Gluza, and J. Eisert, *Proceedings of the National Academy of Sciences* **117**, 26123 (2020).
- [28] E. Kökcü, H. A. Labib, J. K. Freericks, and A. F. Kemper, *Nature Communications* **15**, 3881 (2024).
- [29] R. Kubo, M. Yokota, and S. Nakajima, *Journal of the Physical Society of Japan* **12**, 1203 (1957).
- [30] Z. Cai, R. Babbush, S. C. Benjamin, S. Endo, W. J. Huggins, Y. Li, J. R. McClean, and T. E. O’Brien, *Rev. Mod. Phys.* **95**, 045005 (2023).
- [31] E. Van Den Berg, Z. K. Mineev, A. Kandala, and K. Temme, *Nature Physics* **19**, 1116 (2023).
- [32] Y. Kim, C. J. Wood, T. J. Yoder, S. T. Merkel, J. M. Gambetta, K. Temme, and A. Kandala, *Nature Physics* **19**, 752 (2023).
- [33] A. Miessen, D. J. Egger, I. Tavernelli, and G. Mazzola, *PRX Quantum* **5**, 040320 (2024).
- [34] S. Mangini, F. Tacchino, D. Gerace, D. Bajoni, and C. Macchiavello, *Europhysics Letters* **134**, 10002 (2021).
- [35] K. Mitarai, M. Negoro, M. Kitagawa, and K. Fujii, *Physical Review A* **98**, 032309 (2018).
- [36] M. Schuld, V. Bergholm, C. Gogolin, J. Izaac, and N. Killoran, *Physical Review A* **99**, 032331 (2019).
- [37] J. Spall, *IEEE Transactions on Automatic Control* **37**, 332 (1992).
- [38] L. E. Fischer, M. Leahy, A. Eddins, N. Keenan, D. Ferracin, *et al.*, “Dynamical simulations of many-body quantum chaos on a quantum computer,” (2024).
- [39] N. Bauer, V. Ale, P. Laurell, S. Huang, S. Watabe, D. A. Tennant, and G. Siopsis, *Physical Review A* **111**, 022442 (2025).
- [40] R. Kubo, *Reports on Progress in Physics* **29**, 255 (1966).
- [41] R. Kubo, M. Toda, M. Toda, R. Kubo, N. Hashitsume, N. Saito, and N. Hashitsume, *Statistical Physics II: Nonequilibrium Statistical Mechanics*, Springer Series in Solid-State Sciences (Springer Berlin Heidelberg, 2012).
- [42] J. Hubbard, *Proceedings of the Royal Society of London. Series A. Mathematical and Physical Sciences* **276**, 238 (1963).
- [43] J. Kanamori, *Progress of Theoretical Physics* **30**, 275 (1963).
- [44] M. C. Gutzwiller, *Physical Review Letters* **10**, 159 (1963).
- [45] T. Giamarchi, A. Iucci, and C. Berthod, “Introduction to Many Body Physics,” [https://giamarchi.unige.ch/wp-content/php\\_code/people/thierry.giamarchi/pdf/many-body.pdf](https://giamarchi.unige.ch/wp-content/php_code/people/thierry.giamarchi/pdf/many-body.pdf) (2013), Lecture Notes, University of Geneva.
- [46] P. Jordan and E. Wigner, *Zeitschrift für Physik* **47**, 631 (1928).
- [47] F. Ferrari, A. Parola, S. Sorella, and F. Becca, *Physical Review B* **97**, 235103 (2018).
- [48] M. Karbach, G. Müller, A. H. Bougourzi, A. Fledderjohann, and K.-H. Mütter, *Physical Review B* **55**, 12510 (1997).
- [49] D. Hendry, H. Chen, P. Weinberg, and A. E. Feiguin, *Physical Review B* **104**, 205130 (2021).
- [50] B. Lake, D. A. Tennant, J.-S. Caux, T. Barthel, U. Schollwöck, S. E. Nagler, and C. D. Frost, *Physical Review Letters* **111**, 137205 (2013).
- [51] A. F. Kemper, C. Yang, and E. Gull, *Phys. Rev. Lett.* **132**, 160403 (2024).
- [52] N. L. Diaz, P. Braccia, M. Larocca, J. M. Matera, R. Rossignoli, and M. Cerezo, “Parallel-in-time quantum simulation via Page and Wootters quantum time,” (2024).
- [53] H. Dembinski, P. Ongmongkolkul, *et al.*, “scikit-hep/iminuit,” (2020).
- [54] J. D. Garrett, “garrettj403/scienceplots,” (2021).
- [55] G. Schwarz, *The Annals of Statistics* **6**, 461 (1978).
- [56] G. Vidal and C. M. Dawson, *Physical Review A* **69**, 010301 (2004).
- [57] N. E. Sherman, M. Dupont, and J. E. Moore, *Physical Review B* **107**, 165146 (2023).
- [58] R. Verresen, *Topology and Excitations in Low-Dimensional Quantum Matter*, PhD Thesis, Technische Universität Dresden (2019).
- [59] J.-S. Caux, “The Bethe Ansatz,” (2024).
- [60] M. Knap, A. Kantian, T. Giamarchi, I. Bloch, M. D. Lukin, and E. Demler, *Physical Review Letters* **111**, 147205 (2013).
- [61] E. Rosenberg, T. I. Andersen, R. Samajdar, A. Petukhov, J. C. Hoke, *et al.*, *Science* **384**, 48 (2024).
- [62] S. N. Filippov, S. Maniscalco, and G. García-Pérez, “Scalability of quantum error mitigation techniques: from utility to advantage,” (2024).
- [63] B. Bauer, D. Wecker, A. J. Millis, M. B. Hastings, and M. Troyer, *Physical Review X* **6**, 031045 (2016).
- [64] P. D. Blocher, S. Asaad, V. Mourik, M. A. I. Johnson, A. Morello, and K. Mølmer, *Physical Review A* **106**, 042429 (2022).